CHAPTER -3

Tensile Behaviour of Inconel 617 Alloy

3.1 Introduction

In the present chapter, the tensile behaviour of the Inconel 617 alloy tested in the temperature range from RT to 900^{o}C and at different strain rates from $5x10^{-4}$ s^{-1} to $1x10^{-2}$ s^{-1} is described. Detailed deformation and fracture behaviour is analysed with the help of optical and electron microscopy. Inconel 617 alloy is widely used in high temperature applications such as combustion chamber liner of aircraft gas turbine engines, hot gas ducts and piping, heat exchanger tubes of Very High Temperature gas cooled Reactors (VHTR), super heater and re-heater tubing of the AUSC power plants. Inconel 617, among Ni base super alloys, is the prime candidate material for these applications due to its good mechanical properties and excellent corrosion and oxidation resistance [86-91].

Use of Inconel 617 alloy for the above applications requires understanding of the overall mechanical properties and related deformation mechanisms over a wide range of temperatures under tensile, creep and cyclic loading. However, only limited investigations have been carried out to study the correlation of the mechanical properties and deformation behaviour of this alloy. Tensile deformation behaviour of the Inconel 617 alloy was studied by various investigators [33-40]. Kauomi et al. [34] studied deformation mechanism of the alloy at various temperatures and observed serrations in the stress-strain curves, in the temperature range of 300-800^{o}C. Wright et al. [35, 36] characterized the variation of elevated temperature properties of this alloy with respect to temperature and strain rate and reported occurrence of serrations in the stress-strain curves for temperatures up to 750^{o}C. Mo et al. [37] studied deformation mechanism of this alloy by conducting tensile tests up to 1000^{o}C and reported occurrence of DSA based on serrated flow. They have also studied the strain rate sensitivity of this alloy [38].

Ekaputra et al. [40] also reported DSA in this alloy; however, the controlling mechanisms of DSA, various manifestations of DSA, characterization of deformation behaviour and fracture behaviour were not discussed in detail. DSA has been found to cause deleterious effect on tensile ductility, low cycle fatigue (LCF) life and creep resistance of structural components [92]. In this chapter, results to establish the range of temperature and strain rate for DSA in the Inconel 617 alloy, in solution annealed condition are discussed. Major emphasis is given to characterize dislocation substructures in the specimens tested at different temperatures in the three regions: (i) below the region of DSA (ii) in the region of DSA and (iii) above the region of DSA. Various manifestations of DSA, deformation and fracture behaviour of this alloy, from room temperature (RT) to 900^{o}C have been discussed in detail.

3.2 Methodology

Cylindrical tensile specimens were machined with gauge length and diameter of 15.5 mm and 4.5 mm respectively from the Inconel 617 alloy in solution annealed condition. Solution annealing treatment was carried out by heating samples at 1175^{o}C for 40 minutes followed by water quenching. Tensile tests were performed using 100 kN screw–driven Instron™ Universal Testing Machine (Model: 4206) over a wide range of temperature from RT to 900^{o}C, at strain rates of $5x10^{-4}$ s^{-1}, $5x10^{-3}$ s^{-1} and $1x10^{-2}$ s^{-1}. Fracture ends of the tensile specimens were transversely sectioned, using slow speed circular saw for fractography. Thin transverse slices of 0.2 mm thickness were sectioned from the region close to the fractured ends of the specimen with slow speed diamond cutter to prepare TEM foils.

3.3 Microstructure in As-received and Solution Annealed Condition

Fig. 3.1a shows optical micrograph of the as-received (AR) Inconel 617 alloy comprising mixture of mostly equiaxed fine grains of austenite (γ) and some elongated grains, with large number of precipitates distributed throughout the matrix. The average size of the grains was found to be 5-10 μm. Precipitates can be observed within grains as well as along the grain boundaries. SEM micrograph in Fig. 3.1b shows chromium rich carbides within and along the grain boundaries (shown by arrow). In addition, particles of Ti(C, N) were also observed as shown by circle. Figs. 3.1c and d shows the Energy Dispersive X-ray Spectroscopy (EDS) analysis carried out for the Ti(C, N) particles and carbides observed respectively.

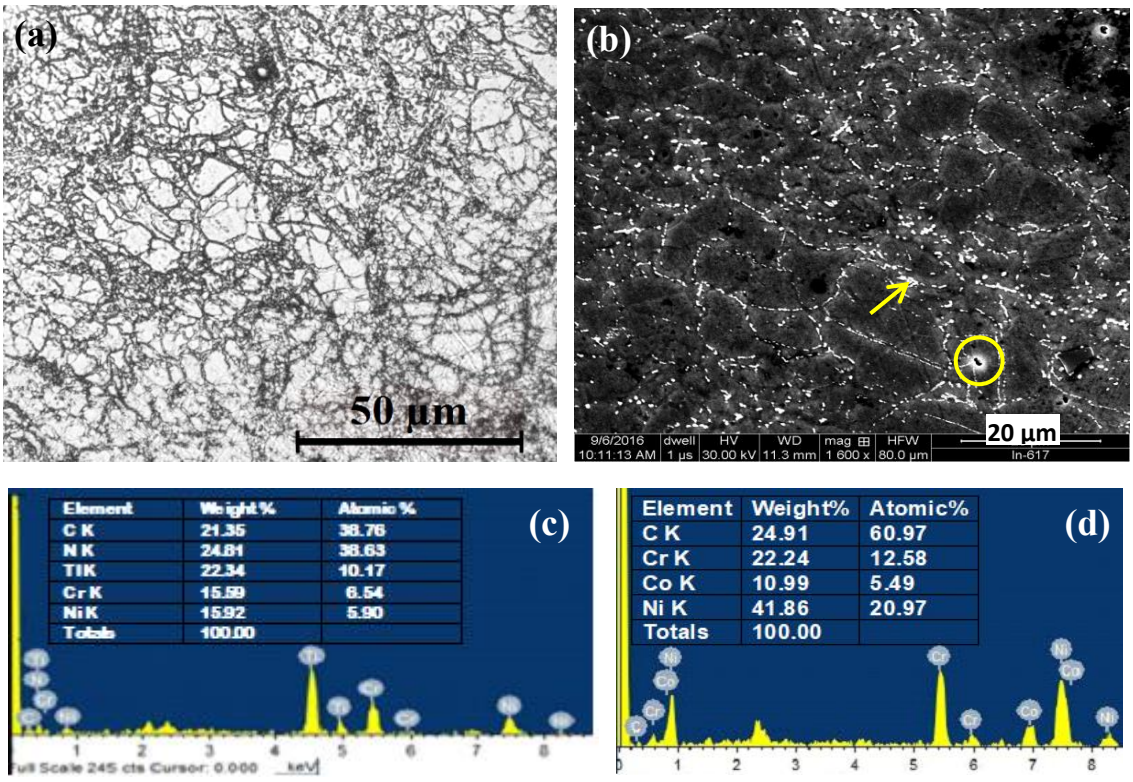

Fig. 3.1: Initial microstructure of the Inconel 617 alloy in the AR condition: (a) Optical micrograph showing fine grains in the matrix along with the precipitates (b) SEM micrograph showing precipitates of Cr rich carbides (indicated by arrow) and Ti (C,N) particles (indicated by circle) (c) EDS analysis of Ti (C,N) particles and (d) EDS analysis of carbides.

Fig. 3.2a displays microstructure of the solution annealed Inconel 617 alloy showing single phase austenitic matrix with dissolution of all the precipitates that were observed in the AR condition. Annealing twins may also be seen in some grains. The average size of the grains was found to be 100 μm. Fig. 3.2b shows SEM micrograph depicting $M_{23}C_6$ carbides along grain boundaries. No precipitates were observed within the grains. This microstructure is similar to that reported by others in solution annealed condition [12, 34]. XRD pattern of the Inconel 617 alloy in solution annealed condition is shown in Fig. 3.3 with peaks of only γ (*fcc*) matrix. Fig. 3.4a shows TEM micrographs of the Inconel 617 alloy in solution annealed condition, indicates the presence of the matrix and precipitates along the grain boundary. The corresponding diffraction pattern to Fig. 3.4a is shown in Fig. 3.4b, which confirms the presence of fine carbide ($M_{23}C_6$, a=10.65Å) precipitates along the grain boundaries of the γ matrix (a=3.608 Å).

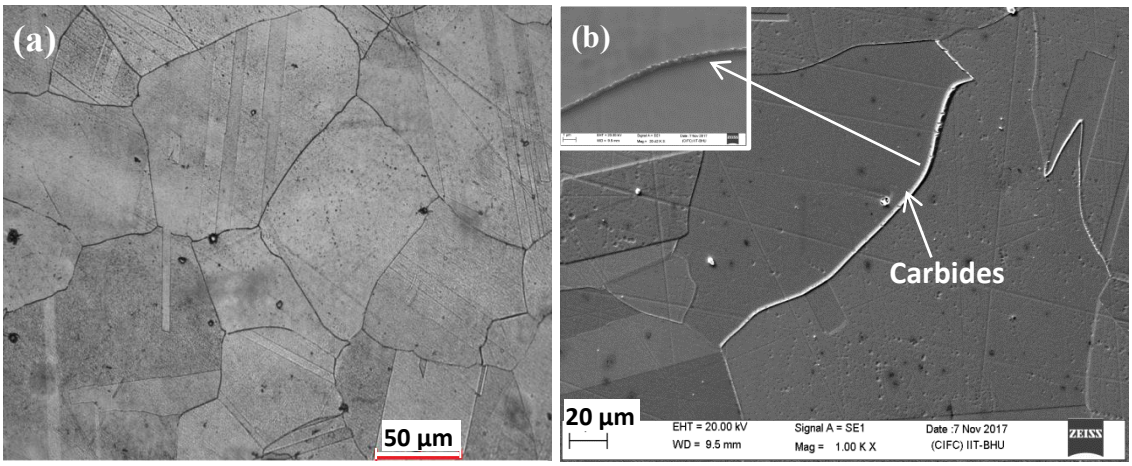

Fig. 3.2: Microstructure of the Inconel 617 alloy in solution annealed (1175°C/40 min/WQ) condition: (a) optical micrograph showing single phase matrix (γ) and annealing twins and (b) SEM micrograph showing decoration of $M_{23}C_6$ (carbide) particles along grain boundaries.

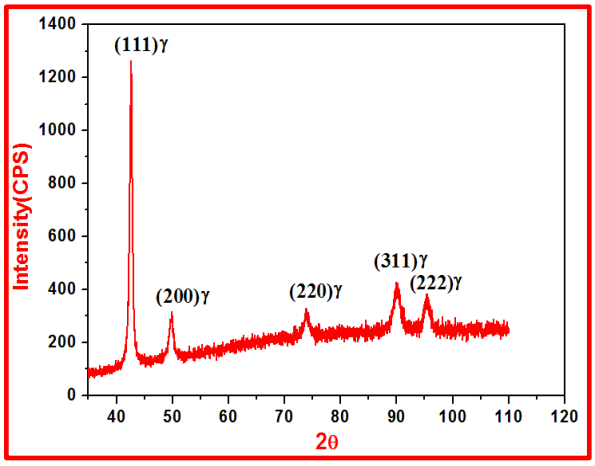

Fig. 3.3: X-Ray diffraction pattern of the Inconel 617 alloy in the solution annealed condition confirming to austenitic matrix.

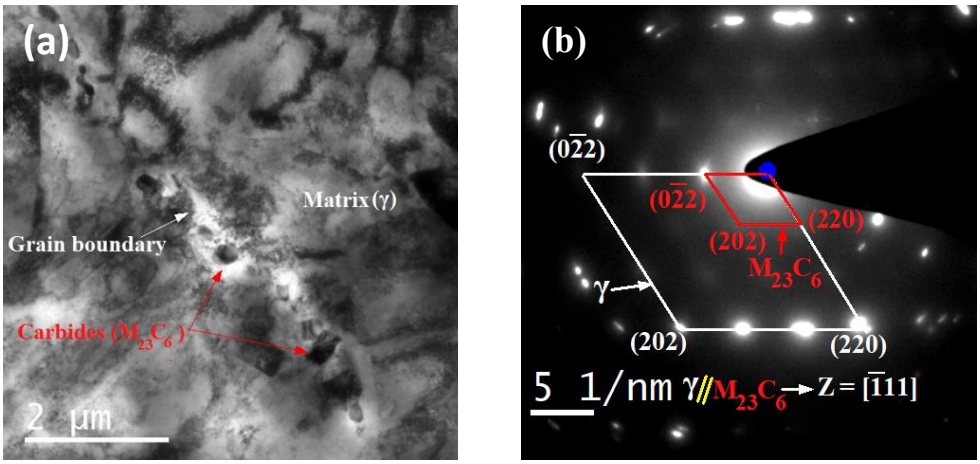

Fig. 3.4: TEM bright field micrographs of the Inconel 617 alloy in solution annealed condition showing: (a) matrix and the $M_{23}C_6$ carbide particles along grain boundaries (b) SAED pattern confirming precipitates as $M_{23}C_6$ carbide (*fcc*) in cube on cube orientation relationship with the matrix (*fcc*).

3.4 Engineering Stress-Strain Curves

Tensile engineering stress-strain curves of the Inconel 617 alloy in solution annealed condition tested at different temperatures from room temperature (RT) to 900°C, at the strain rates ($\dot{\varepsilon}$) of $5x10^{-4}$ s^{-1}, $5x10^{-3}$ s^{-1} and $1x10^{-2}$ s^{-1} are shown in Fig. 3.5a, 3.5b & 3.5c respectively. Magnified view of the stress strain curves obtained at the

strain rate of $5x10^{-3}$ s^{-1} is displayed in Fig. 3.5d. Serrated plastic flow can be seen in the curves corresponding to the test temperatures from 300^{o}C to 600^{o}C at all the strain rates studied. Although the magnified stress-strain curves show some jerky flow at 200^{o}C and after the yield point at 700^{o}C, significant load drop was not observed and very weak tendency of serration is only noticed. Serrations at the low temperature of 300^{o}C are predominantly of type B. At 400^{o}C and 500^{o}C, there are (A+B) type and at 600^{o}C, C type serrations are noticed. Type C serrations are observed at 500^{o}C at the strain rate of $5x10^{-4}$ s^{-1}. Type A serrations are characterized by periodic serrations, with abrupt rise of stress followed by a drop of stress in the stress-strain curve at intervals of strain. Type B serrations are characterized by continuous oscillations of stress in the stress–strain curve, while type C serrations exhibit abrupt irregular stress drops [31].

In the present study, serrations in the stress–strain curves appeared almost from the beginning of the plastic deformation and continued till the attainment of ultimate tensile strength, and over the temperature range from 300 to 600°C. The amplitude of serrations increased with decrease in the strain rate and increase in temperature.

3.5 Variation of Critical Plastic Strain

The critical plastic strain (ε_c) for the onset of serrated flow, calculated from the true stress–true strain curves, is the minimum plastic strain at which a perceptible stress drop of 0.5 MPa occurs [93]. The variations of the critical plastic strain (ε_c) with strain rate and temperature are shown in Fig. 3.6a & b respectively. The amount of critical plastic strain required for the onset of serrations is found to be decreased with increase in the temperature and decrease in strain rate. The critical plastic strain between 400^{o}C to 600^{o}C is observed to be minimum and remain stable at higher temperatures. It is also interesting to note that the magnitude of ε_c is relatively higher at the higher strain rates

at constant temperature (Fig. 3.6b).

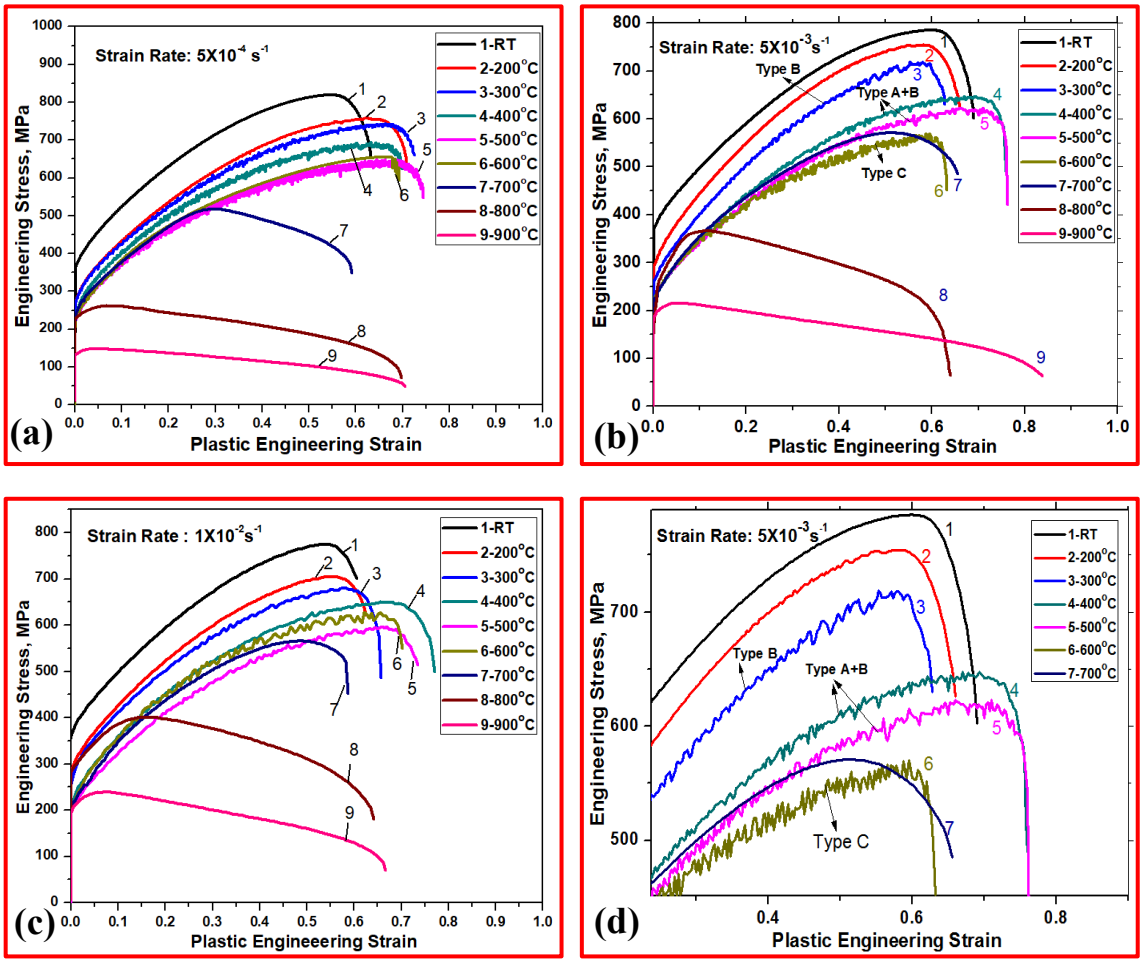

Fig. 3.5: Engineering stress–strain curves of the Inconel 617 alloy in solution annealed condition tested at different temperatures and at strain rates of: (a) 5x10^{-4} s^{-1}, (b) 5x10^{-3} s^{-1}, (c) 1x10^{-2} s^{-1} and (d) magnified view of serrations at strain rate.

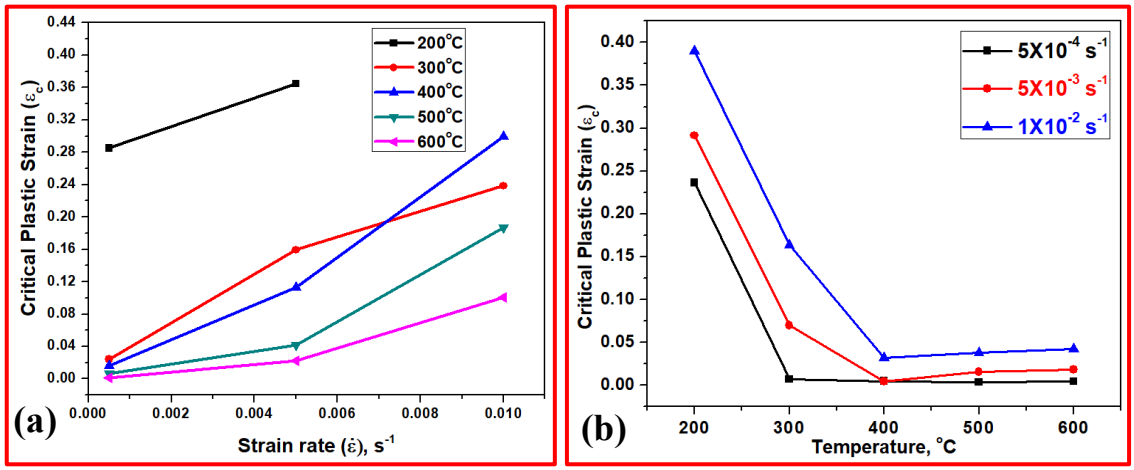

Fig. 3.6: Variation of critical plastic strain for the onset of serrations with: (a) strain rate and (b) temperature.

3.6 Variation of Strength and Elongation with Temperature

Tensile properties of the Inconel 617 alloy in solution treated condition tested at various temperatures and at the intermediate strain rate of $5x10^{-3}$ s^{-1} are shown in Table 3.1. The variation of 0.2% offset yield strength (YS) with temperature at the three different strain rates is shown in Fig. 3.7a. The yield strength continuously decreased with increase in temperature at all the strain rates up to 700°C while there is an increase at 800°C followed by rapid decrease at 900°C. The rate of fall of the yield strength was relatively low from 400 to 700°C as indicated by the plateau in the highlighted portion. There is stability (plateau) in the temperature range from 400°C to 700°C at all three strain rates studied and it could be due to occurrence of DSA. The effect of strain rate is clearly visible as there is a decrease in the YS with increase in the strain rate from 300°C to 700°C, and thereafter, normal behaviour is observed.

Table 3.1: Tensile Properties of Inconel 617 Alloy in Solution Annealed Condition Tested at Various Temperatures at Strain Rate of $5x10^{-3}$ s^{-1}.

Temperature °C	0.2% Y.S, MPa (S_{YS})	U.T.S, MPa (S_{UTS})	% Elongation (e_f)	% R.A.	Serration	Degree of work hardening (S_{UTS}/S_{YS})
RT	385	805	67	52	Not Found	2.09
200	285	754	64	62	Not Found	2.64
300	261	728	67	60	Type B	2.75
400	231	663	72	63	Type A+B	2.87
500	226	638	73	60	Type A+B	2.82
600	223	583	59	40	Type C	2.61
700	217	570	61	46	Not found	2.62
800	250	365	70	72	Not found	1.46
900	190	217	87	75	Not found	1.09

The effect of temperature on the ultimate tensile strength at the three strain rates is presented in Fig. 3.7b. The ultimate tensile strength continuously decreases with

increase in temperature for all the three strain rates studied, with the degree of fall being rapid above 700°C. The UTS is higher at increased strain rates. The true stress (σ) required to maintain the plastic deformation at the particular true strain was calculated from the true stress-true strain diagram corresponding to the strain of ε =0.1 and the variation of σ with temperature is shown in Fig. 3.7c. It indicates continuous decrease in σ with temperature and peaks at 600°C and again at 800°C which is a typical manifestation of DSA. There is a transition in the values of flow stress (σ) from 300 to 700°C with respect to the strain rate.

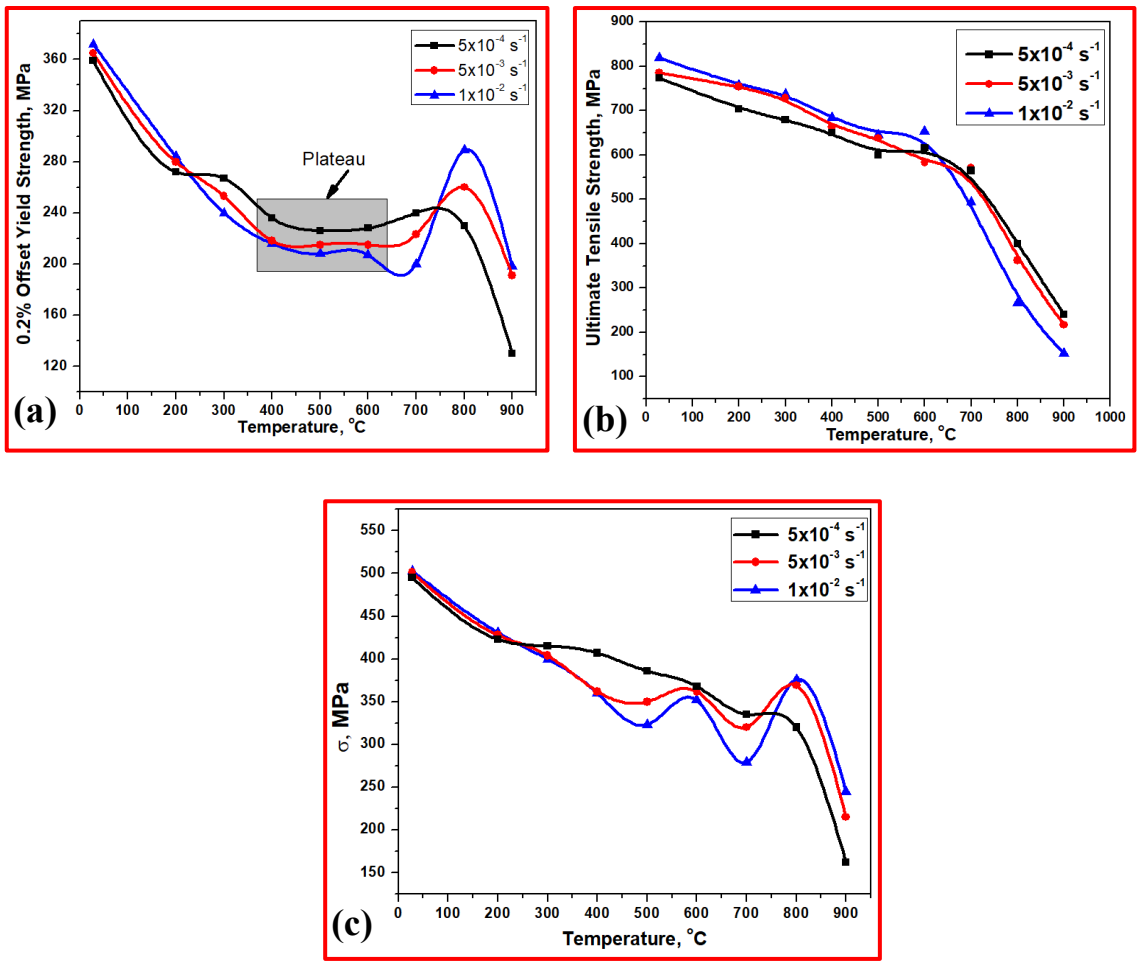

Fig. 3.7: Effect of temperature and strain rate on (a) 0.2% offset yield strength (b) ultimate tensile strength and (c) flow stress (σ) at ε =0.1.

The effect of temperature on the total elongation is shown in Fig. 3.8a. The total elongation increased from room temperature to 400°C and is followed by decrease up to 700°C and again by increase at higher temperatures. At all the three strain rates, the elongation decreased from 400°C to 700°C which could be due to the DSA [31]. There is an increase in the elongation from 800°C to 900°C. The variation of the uniform plastic strain (plastic strain up to the ultimate tensile strength, e_{pu}), with temperature is shown in Fig. 3.8b, which drops in the temperature range from 400°C to 700°C.

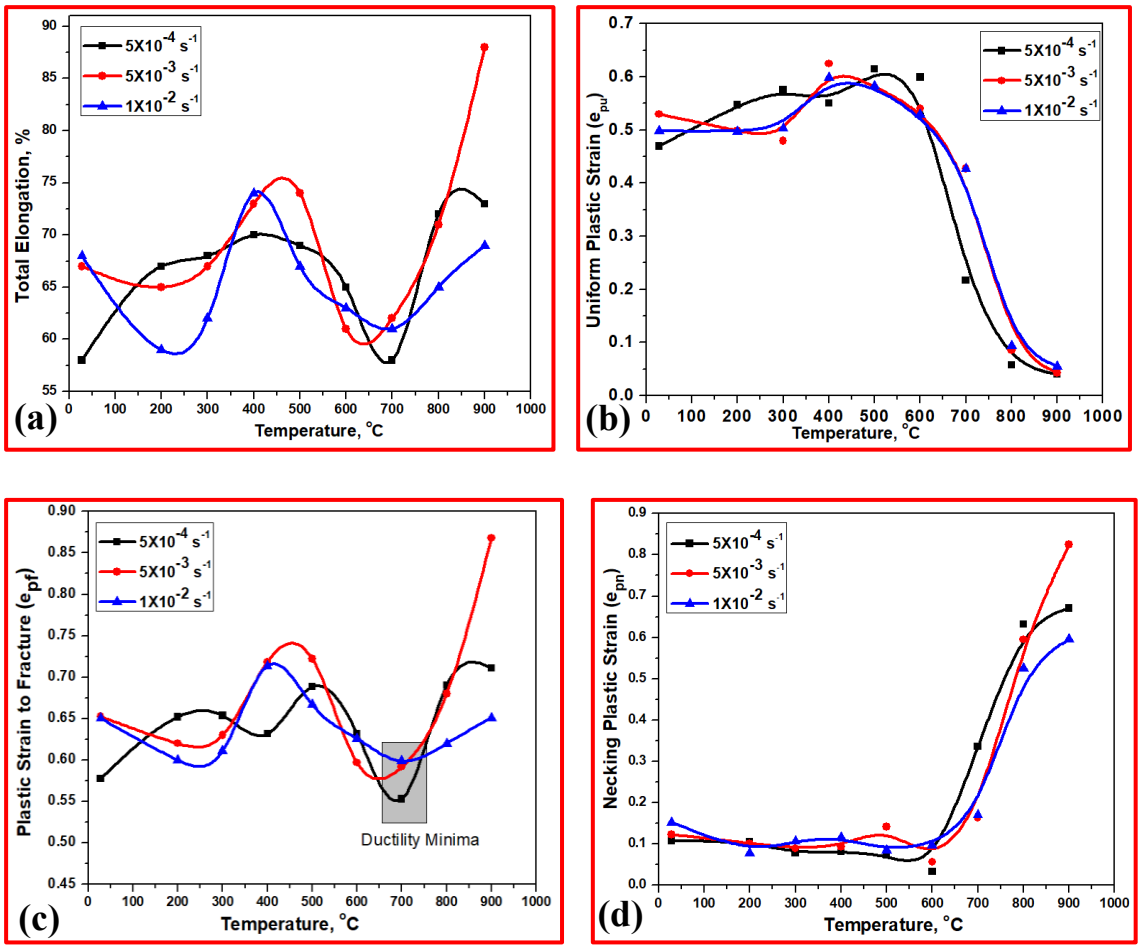

Fig. 3.8: Effect of temperature and strain rate on (a) total elongation (b) uniform plastic strain (e_{pu}) (c) plastic strain to fracture (e_{pf}) and (d) necking plastic strain (e_{pn}).

The variation of plastic engineering strain to fracture (e_{pf}) with temperature, at the three different strain rates is shown Fig. 3.8c. The e_{pf} shows minima at 600°C and

700^{o}C for all the three strain rates. On the other hand, the variation of the engineering necking plastic strain (strain from maximum tensile stress to fracture stress, e_{pn}), with temperature shows noticeable minima for different strain rates at 600^{o}C (Fig. 3.8d). The variation in the e_{pn} is not much but after 700^{o}C, there is sudden increase in the necking plastic strain. The degree of work hardening (S_{UTS}/S_{YS}) (Table 3.1) gradually increased up to 500^{o}C and thereafter decreased up to 900^{o}C.

3.7 Variation of Strain Rate Sensitivity with Temperature

Strain rate sensitivity (m), at a given temperature (T) and true strain (ε) was calculated using the σ - ε data from the tensile tests at constant cross head speeds. 'm' was calculated from the flow stress at different true strains using the relationship:

$$m = \log (\sigma_2/\sigma_1)/\log (\dot{\varepsilon}_2/\dot{\varepsilon}_1) \quad \text{----------} \quad (3.1)$$

where σ_1 and σ_2 are true stresses corresponding to the true strain rates $\dot{\varepsilon}_1$ and $\dot{\varepsilon}_2$ respectively [94].

The strain rate sensitivity(m) was determined at ε = 0.1 from the flow stresses corresponding to strain rates $\dot{\varepsilon}_1$ and $\dot{\varepsilon}_2$ and the variation of 'm' with temperatures is shown in Fig. 3.9. The values of 'm' are positive and very low up to 200^{o}C. From 300^{o}C to 700^{o}C, 'm' values are negative at which serrations are observed in the stress strian curves. However, at 800^{o}C the 'm'values are positive, and increased up to 900^{o}C. This is another manifestation of DSA in this alloy, which clearly identifies the temperature range of DSA. The 'm' values are comparable with those reported J. Wright et al [36] for the Inconel 617 alloy.

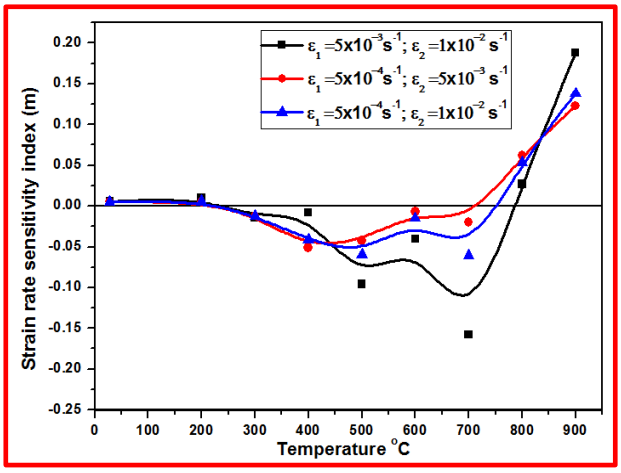

Fig. 3.9: Effect of temperature on strain rate sensitivity (*m*).

3.8 Variation of Work Hardening Parameters with Temperature

Various relationships were proposed by different investigators to characterize work hardening behaviour of materials. Hollomon, Ludwigson, Ludwik, Swift and Voce relationships are well known [41-45] and the validity of these equations is checked for the Inconel 617 in the present investigation. Fig. 3.10a shows log-log plots of true stress *vs* true plastic strain in the region of uniform plastic strain, for the samples tested at RT, 400^{o}C, 700^{o}C and 900^{o}C. At room temperature, 400^{o}C and 700^{o}C the curves clearly show upward concave curve whereas at 900^{o}C straight line was observed. The flow behaviour of the present alloy was analyzed using the above five relationships for their validity and to find out various work hardening parameters at all the temperatures. The log-log plots of true stress and true plastic strain for the samples tested at all the temperatures were fitted with linear regression analysis using different equations with help of software and the curves obtained are shown in Figs. 3.10b, c and d as superimposed curves.

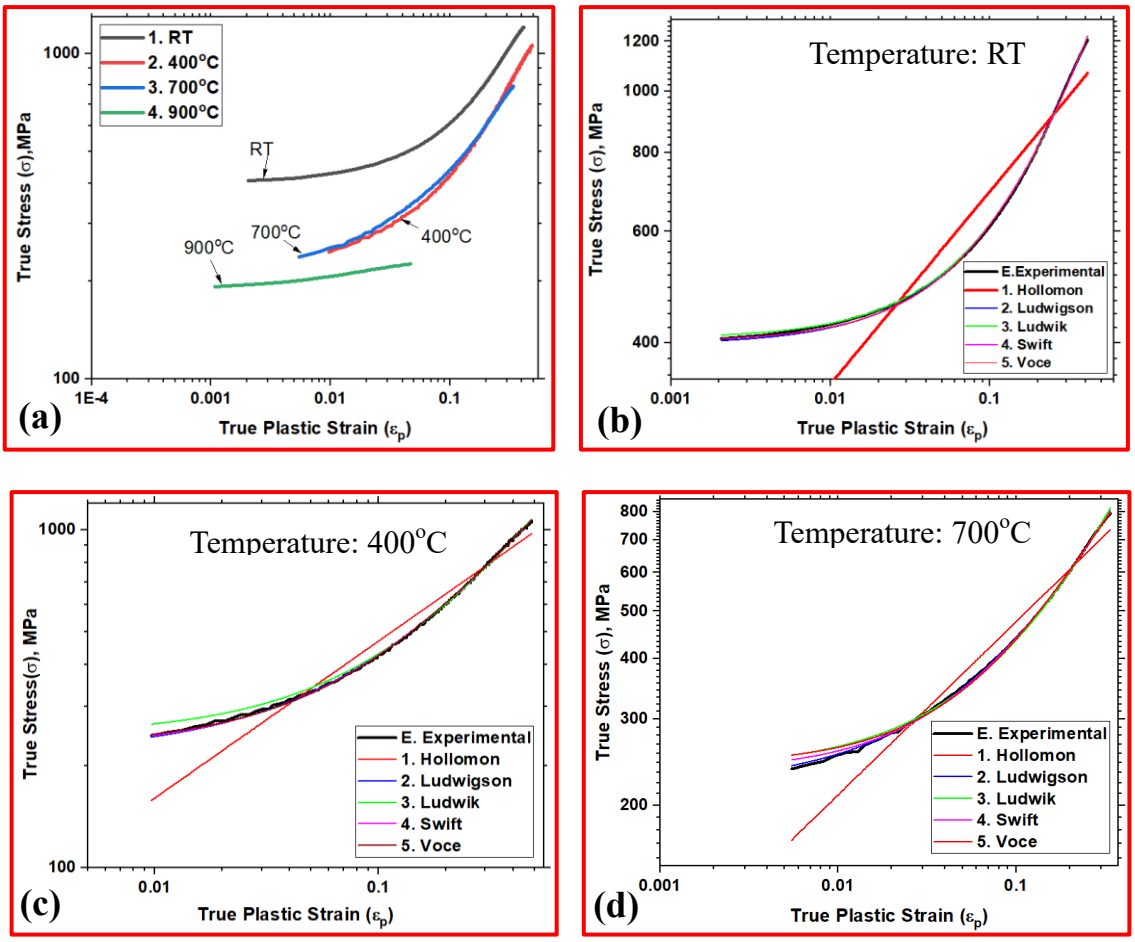

Fig. 3.10: (a) Log-log plots of the true stress- true plastic strain at different temperatures, and validity of various flow equations: (b) for the sample tested at RT (c) for the sample tested at 400°C and (d) for the sample tested at 700°C.

Ludwigson equation is found to be the best to describe the work hardening behaviour of the Inconel 617 alloy from RT to 700°C. However, at the higher temperature, Hollomon relationship is found to be fit. Various work hardening parameters calculated using the Ludwigson equation [42]

$$\sigma = K\varepsilon^{n} + \exp(K_1 + n_1\varepsilon) \quad \text{----------} \quad (3.2)$$

are shown in the Table 3.2. The transition strain (ε_L) was evaluated by setting the value of the ratio r, ($r = \exp(K_1+n_1\varepsilon)/K\,\varepsilon^{n}$), to as small value as possible near zero. The transition strain (ε_L) and the corresponding transition stress (σ_L) were determined for two different values of r, 0.001 and 0.002 respectively. The transition values of σ_L are

presented in Table 3.2, which show decrease in σ_L with increase in temperature, while the values of ε_L are found to be within the range of 0.153-0.212, with no specific trend with respect to temperature.

Table 3.2: Strain Hardening Parameters Derived from Ludwigson Equation at Various Temperatures.

Temperature ^oC	***K***	***n***	K_1	$-n_1$	***r* = 0.001**		***r* = 0.002**	
					ε_L	σ_L	ε_L	σ_L
28	2095	0.634	5.86	14.21	0.212	838	0.198	828
200	2030	0.607	5.58	14.91	0.192	732	0.189	720
300	2015	0.717	5.53	13.03	0.189	628	0.178	615
400	1768	0.711	5.37	13.10	0.202	607	0.195	600
500	1661	0.690	5.36	12.76	0.183	560	0.175	555
600	1494	0.641	5.32	12.65	0.199	557	0.187	540
700	1539	0.643	5.24	14.67	0.153	528	0.142	523
800	1423	0.582	Hollomon equation					
900	300	0.083	Hollomon equation					

The variation of *K* and *n* with temperature is shown in Fig. 3.11a &b respectively. *K* and *n* continuously decreased from RT to 900^{o}C, though the drop is more drastic from 700^{o}C to 900^{o}C. The values of *K*, *n* in the temperature range 400-600^{o}C exhibit little variation, in the region of DSA. The *K* value also decreased gradually with strain rate. The magnitude of *n* ranged between 0.6 and 0.75 for all the strain rates studied. The work hardening parameters obtained are in agreement with the data reported for the austenitic stainless steel [95].

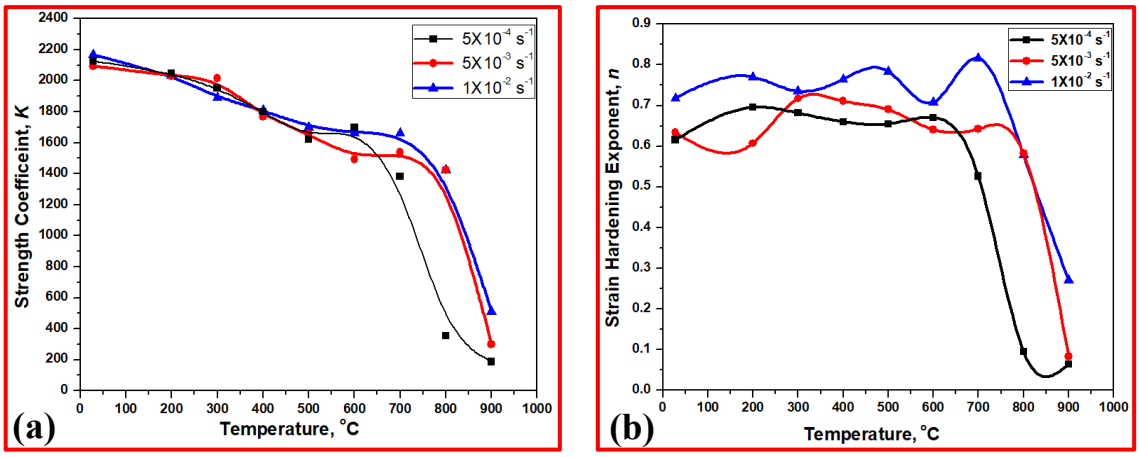

Fig. 3.11: Variation of (a) strength coefficient (K) and (b) strain hardening exponent (n), with temperature at different strain rates.

Peaks in the variation of work hardening rate ($\theta=d\sigma/d\varepsilon$) with temperature is another anomaly observed due to DSA. The work hardening behaviour of this alloy and different stages of work hardening rate are discussed in detail in Chapter 4. Fig. 3.12 shows the variation of θ with temperature, it can be observed that well defined peaks around 500°C and 700°C for the strain rates of $5x10^{-3}$ s^{-1} and $1x10^{-2}$ s^{-1}, whereas at the strain rate of $5x10^{-4}$ s^{-1}, peak is observed only at 700°C. This is one of the manifestations of DSA.

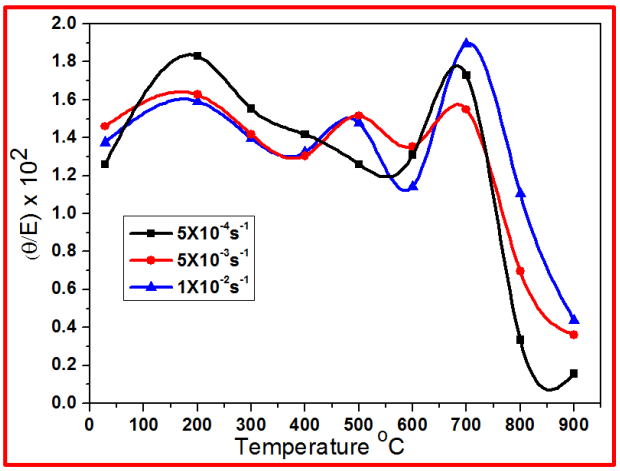

Fig. 3.12: Variation of normalised work hardening rate (θ/E) with temperature at three strain rates [E is Young's modulus, $\theta = \Delta\sigma/\Delta\varepsilon$, where $\Delta\sigma$ is the flow stress increment over the strain interval $\Delta\varepsilon$ from $\varepsilon = 0.1$ to $\varepsilon = 0.2$].

3.9 Determination of Activation Energy

Three different methods have been employed to evaluate the activation energy for the serrated flow [93, 94, 96-98]. In the first method, known as Cottrell's approach [96], variation of the critical plastic strain (ε_c) with strain rate ($\dot{\varepsilon}$) and temperature (T) was plotted to calculate the activation energy. The exponent ($m+\beta$) was obtained from the slope of the plot of ln $\dot{\varepsilon}$ *vs* ln ε_c at a constant temperature. The slope of the plot of ln ε_c *vs* $1/T$ at constant $\dot{\varepsilon}$ was used to evaluate Q using the relationship,

Q = slope x ($m+\beta$) x R ---------- (3.3)

where R is the universal gas constant. The second method is based on the McCormick's quasi-static strain ageing model [97], which relates the concentration dependence of ε_c with temperature. In the third method, the value of Q is determined from the load-drop measurements as suggested by Pink and Grinberg [98].

Fig. 3.13a shows the variation of ln $\dot{\varepsilon}$ with ln ε_c to calculate activation energy by the method 1(Cottrell's approach), the average value of the slope of the plot ($m+\beta$) over the temperature was 0.99 and the activation energy (Q) was 61 kJ/mol determined using the slope of the plot of ln ε_c vs 1/T (Fig. 3.13b). The activation energy (Q) determined by the method 2 from the plot of ln $\varepsilon_c^{(m+\beta)}$/T *vs* 1/T, was found to be 74 kJ/mol (Fig. 3.14).

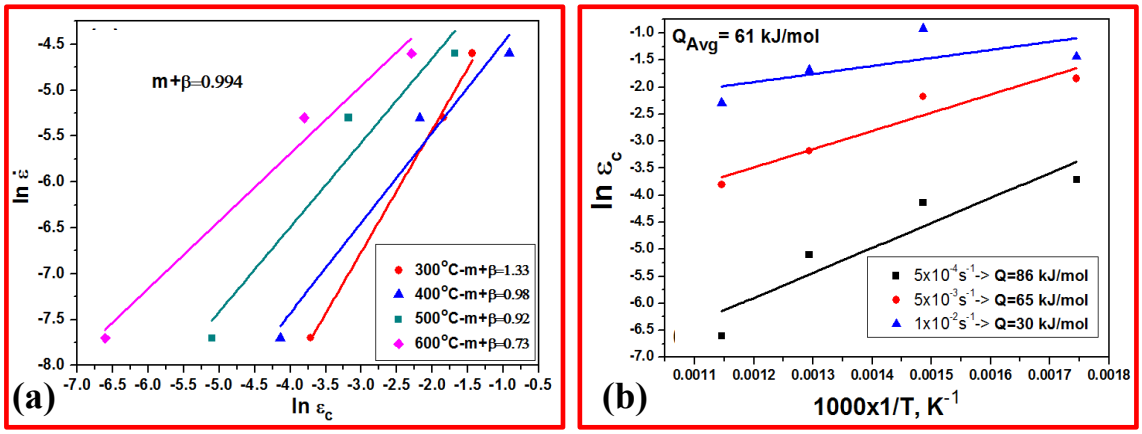

Fig. 3.13: (a) Variation of ln $\dot{\varepsilon}$ with ln ε_c (true critical plastic strain). The value of the slope ($m+\beta$) was used to calculate the activation energy (Q = 61 kJ/mol) and (b) ln ε_c vs 1/T plots to calculate activation energy by Cottrrel's approach [Method 1].

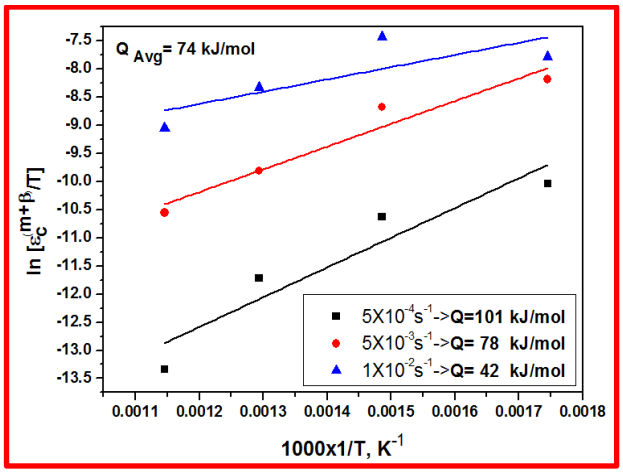

Fig. 3.14: ln $\varepsilon_c^{(m+\beta)}$/T vs 1/T plot to calculate activation energy using McCormick method [Method 2].

Fig. 3.15a shows the plots of $\dot{\varepsilon}$ *vs* $\Delta\sigma_{Avg}$ for 300°C and 400°C. The intercepts of $\dot{\varepsilon}$ at both the temperatures for $\Delta\sigma_{Avg}$ values of 12 and 16 MPa were determined from Fig. 3.15a and are plotted in the Fig. 3.15b as the plot of ln $\dot{\varepsilon}$ *vs* 1/T, slopes of which were used to determine Q. Similar procedure was followed for the test temperatures of 500 and 600°C (Figs. 3.16a &b). The values of Q calculated using the method 3 are 34 kJ/mol, 84 kJ/mol, 58 kJ/mol and 55 kJ/mol for 300°C, 400°C, 500°C and 600°C respectively. The comparison of the values of activation energy estimated using the

three methods is shown in Table 3.3. The methods 1, 2 and 3 are described in detail in earlier reports [96, 97 and 98]. The Q values obtained are in accordance with the values reported by Han et al. [93] for various nickel base superalloys.

Table 3.3: Activation Energies for DSA Calculated by Different Methods for the Inconel 617 Alloy.

Method	Strain rate	Q, kJ/mol	$m+\beta$
Method 1 (Cottrell's) [96]	$5x10^{-4}$ s^{-1}	86	0.994
	$5x10^{-3}$ s^{-1}	65	
	$1x10^{-2}$ s^{-1}	30	
Method 2 (McCormick's)[97]	$5x10^{-4}$ s^{-1}	101	
	$5x10^{-3}$ s^{-1}	78	
	$1x10^{-2}$ s^{-1}	42	
Method 3 (Load drop) [98]	NA	58	-

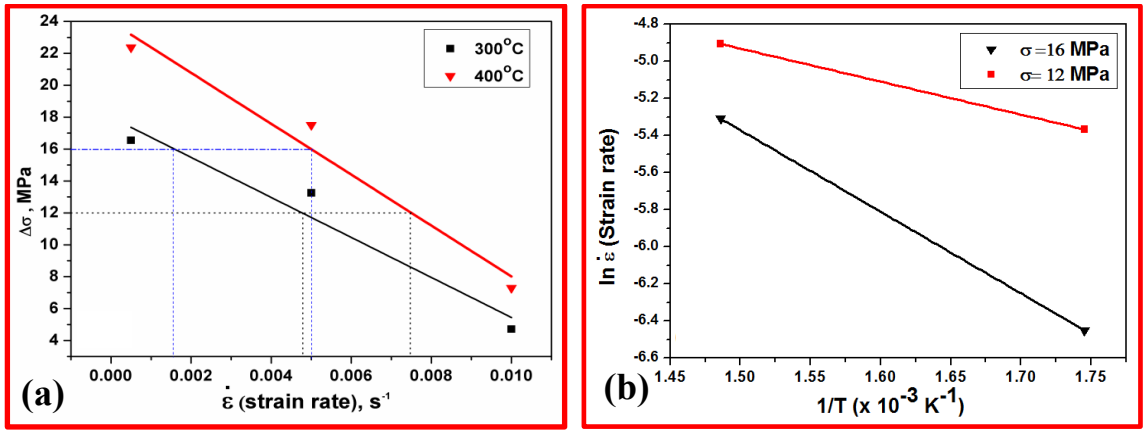

Fig. 3.15: (a) $\dot{\varepsilon}$ *vs* $\Delta\sigma$ plots for 300°C and 400°C and (b) ln $\dot{\varepsilon}$ *vs* 1/T plots to calculate activation energy using stress drop method [Method 3].

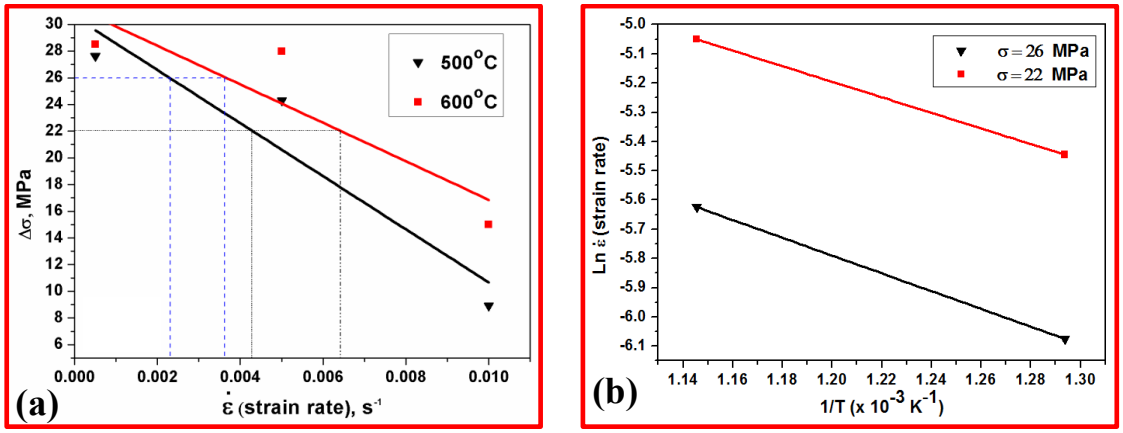

Fig. 3.16: (a) $\dot{\varepsilon}$ *vs* $\Delta\sigma$ plot for 500°C and 600°C and (b) ln $\dot{\varepsilon}$ vs 1/T plots to calculate activation energy by stress drop method [Method 3].

3.10 Deformation Behaviour

The slip characteristics and dislocation substructure of the tensile specimens of Inconel 617 in solution annealed condition tested from room temperature (RT) to 900^{o}C at the strain rate of 5x10^{-3} s^{-1} were characterized, in order to examine the differences in dislocation substructure and slip-band formation. Fig. 3.17a shows the deformed microstructure of the sample tested at RT exhibiting smooth flow without serrations, in which traces of coarse slip bands can be seen. The width of the slip bands (w) is around 0.6 to 0.8 μm. There are tangles of high density of dislocations in the slip bands (Fig. 3.17b). The microstructure comprises of small and thick walled cells, formed due to the mutual annihilation of dislocations, and reorganisation of the remaining dislocations into a low energy structure. Dislocation pileups at low temperatures could be attributed to less extent of plastic deformation at the ambient temperature. Similar observations were made for the sample tested at the 200^{o}C.

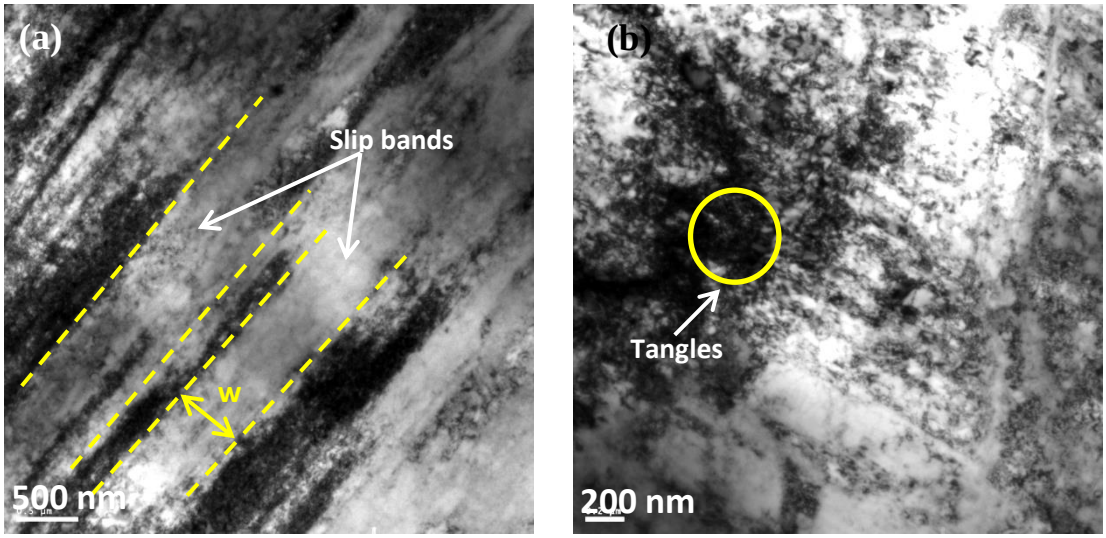

Fig. 3.17: TEM micrographs of solution annealed tensile samples of the Inconel 617 alloy tested at room temperature at a strain rate of 5x10^{-3} s^{-1} showing: (a) slip bands and (b) tangles of dislocations.

Fig. 3.18a shows deformation structure of the sample tested at 400^{o}C, at which serrations or jerky flow was observed, the number of slip bands may be seen to increase and the slip width (w) to decrease to 0.3-0.5 μm with increase in temperature. The crossing of slip bands due to activation of other variants of slip planes of the same family can also be seen. Fig. 3.18b shows significant increase in the tangles of dislocations within the cells with respect to that tested at room temperature. It is important to mention that these cells are elongated in shape unlike those in samples tested at RT.

The pinning path of the dislocations is quite evident from Fig. 3.18c (as shown by arrows) and also evident is bending of the path due to the obstruction for the movement of the dislocation at several places along its line vector. Formation of dislocation kinks (*k*), dislocation loops and bowing (*b*) of dislocations (shown by arrows), resulting from pinning of dislocations is clearly manifested in the microstructure shown in Fig. 3.18d.

In order to understand the mechanism during serrated flow, one interrupted tensile test (up to ε = 0.4) was carried out at 400^{o}C and at the strain rate of 5x10^{-3} s^{-1}. Fig. 3.19a shows the deformation structure of this sample, indicating more number of pinning locations and clear picture of bowing path of the movement of dislocations at several places. Fig. 3.19b shows multiple pinning centres identified as dark spots (see at arrows), revealing the fact that there is an interaction of dislocations with solute atmospheres. One such location of this pinning viewed under high resolution to confirm the mechanism is shown in Fig. 3.19c. The dark contrast in the image in addition to that due to the stress field of the dislocation, is arising due to the clustering of solute atoms on to the dislocation. No clear boundary is associated with this feature since it is only a clustering of solute without forming any precipitate (Fig. 3.19d). The image confirms

the solute atoms interaction with dislocations during serrated flow. The nature and type of the solute atoms cannot be distinguished by this experiment. However, at the temperature regime at which the test was carried out, it is understood that substitutional solute atoms cluster to the core of the dislocation. According to the theory of DSA, the interaction between dislocations and solute atoms limits the freedom of motion of dislocations. The pinned portions of the dislocations minimise the ability of dislocations to cross slip.

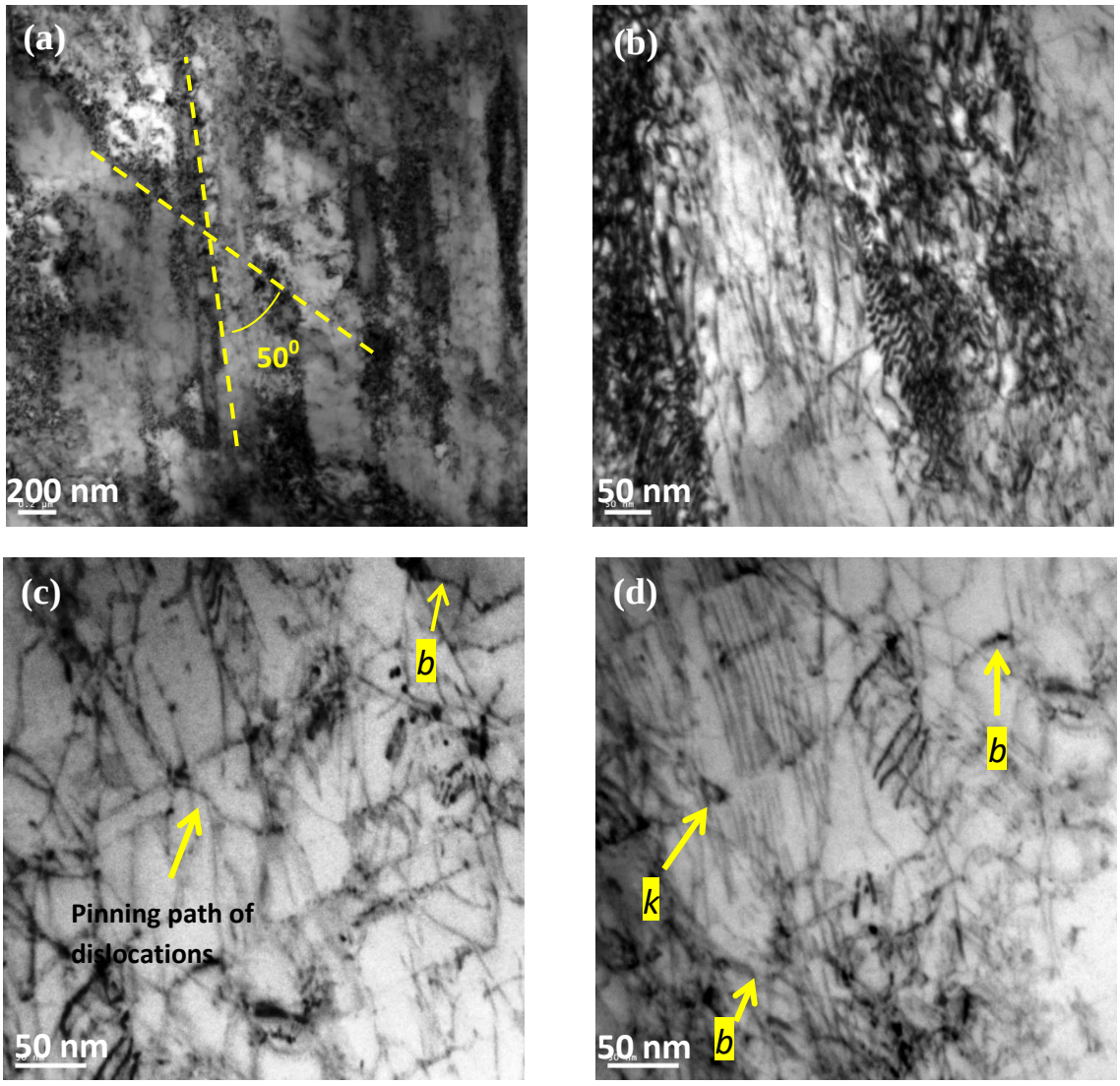

Fig. 3.18: TEM micrographs of tensile samples tested at 400^{o}C (exhibiting serrrated flow), at a strain rate of 5x10^{-3} s^{-1} showing: (a) cross slip bands of same slip system. Number of slip bands are more compared to the sample tested at lower temperature, (b) alignment of dislocations within the slip band, (c) arrows indicate pinning path of the dislocations represented by dark black spots anchoring the dislocation and bowing and (d) arrangement of dislocations in pairs (*k*-kinks, *b*-bowing of dislocations).

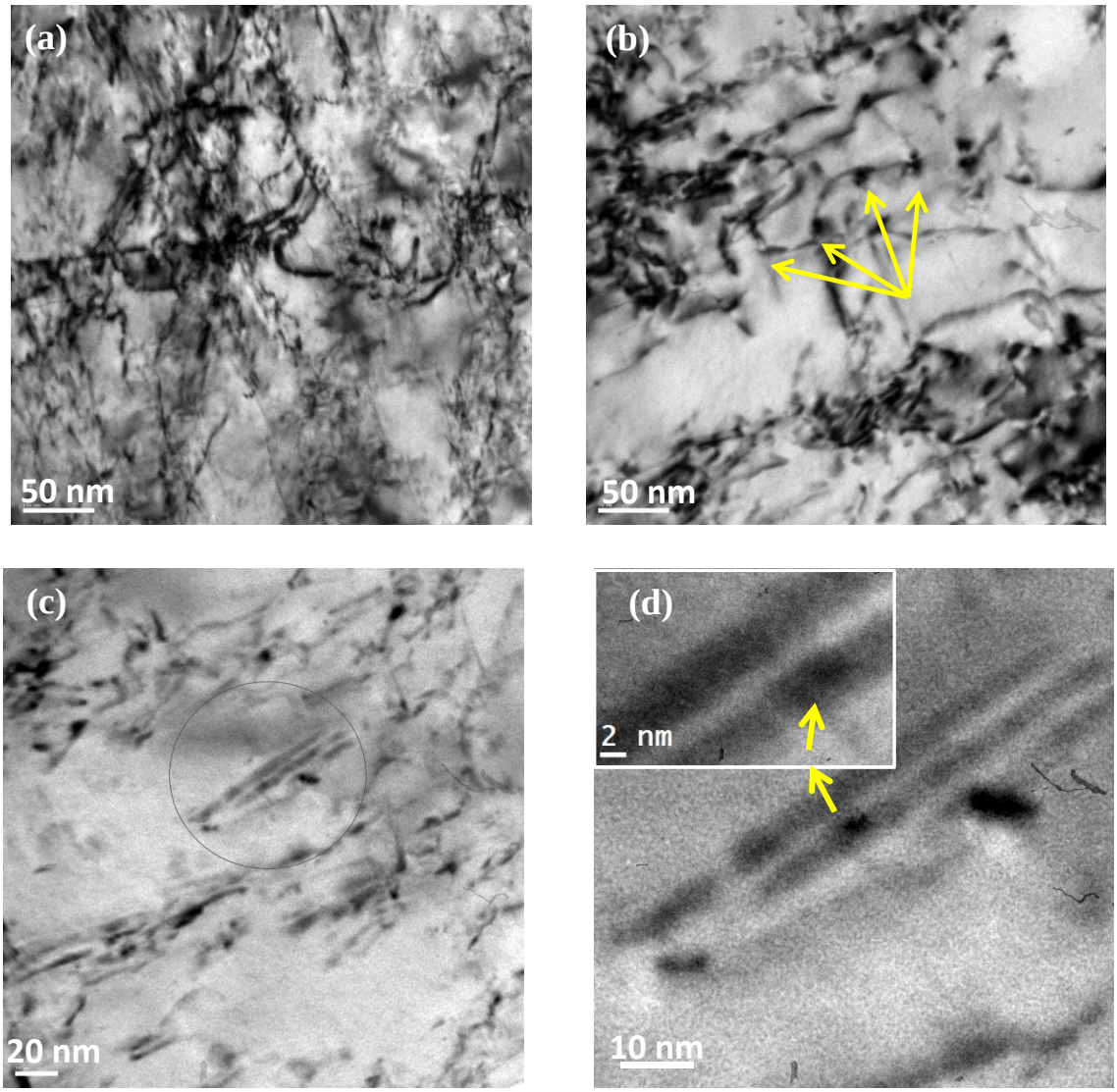

Fig. 3.19: TEM micrographs of tensile sample tested at 400^{o}C and at strain rate of 5x10^{-3} s^{-1}- test interrupted at ε = 0.4, (continuing serrated flow) showing: (a) more number of pinning locations for dislocations compared to that of samples tested up to fracture (b) multiple pinning locations of dislocations as indicated by arrows (dark spots) (c) clustering of solute atoms to the core of the dislocation and (d) high resolution image of the cluster of heavy atoms indicated by the contrast (see at the arrow).

During DSA, at the higher temperature, solute atoms diffuse with higher velocity and form saturated solute atmosphere surrounding the dislocations and thus restrict the glide of dislocations on particular planes. This occurs due to inherent instability of the position that separates the fast slip region from the slow slip region in the slipped zone [31]. In order to unpin the dislocations from the atmosphere of interstitial solutes for

further deformation, the applied stress needs to be increased, which further increases the density of dislocations. Another alternative is to increase the temperature whereby the solute atmosphere diffuse out into the matrix lattice.

Fig. 3.20a shows TEM micrographs of the samples tested at 600^{o}C, at which the number of slip bands increased and slip band width further decreased to around 0.05-0.1 μm. Here cross slip bands are not observed, the bands are much narrower and have narrow boundaries in which few dislocations are bounded, thus the dislocation density within the slip bands was decreased. Formation of dislocation loops and bowing of dislocations occurred resulting from pinning of dislocations at this temperature also (Fig. 3.20b).

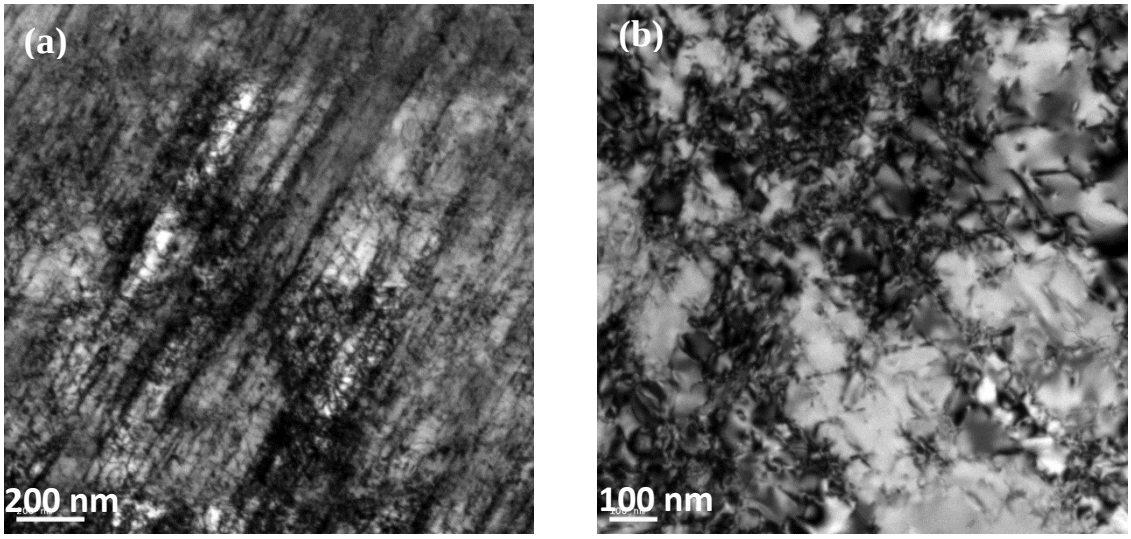

Fig. 3.20: TEM micrographs of tensile samples tested at 600^{o}C, (exhibiting serrated flow) at a strain rate of 5x10^{-3} s^{-1} showing: (a) more number of slip bands compared to that tested at 400^{o}C and (b) high density of dislocations.

Fig. 3.21a shows deformed microstructure of the sample tested at 700^{o}C that exhibited low amplitude serrations. Interestingly, no traces of slip bands were observed, unlike those in the samples tested at RT and the others tested in the DSA regime. There is an indication of formation of precipitates, linearity of dislocations and a lower

dislocations density. Fig 3.21b shows micro twins in the microstructure and indicates deformation by twinning. Burke et al. [61] observed similar micro twins in the samples tested under low cycle fatigue conditions, at 870^{o}C in this alloy. Fig. 3.21c shows the precipitates of $M_{23}C_6$ and γ′, identified by the selected area electron diffraction pattern (SAED) shown in Fig. 3.21d. The precipitation of the second phase particles enhanced the rate as well as the degree of work hardening, due to which both uniform as well as elongation to fracture were reduced.

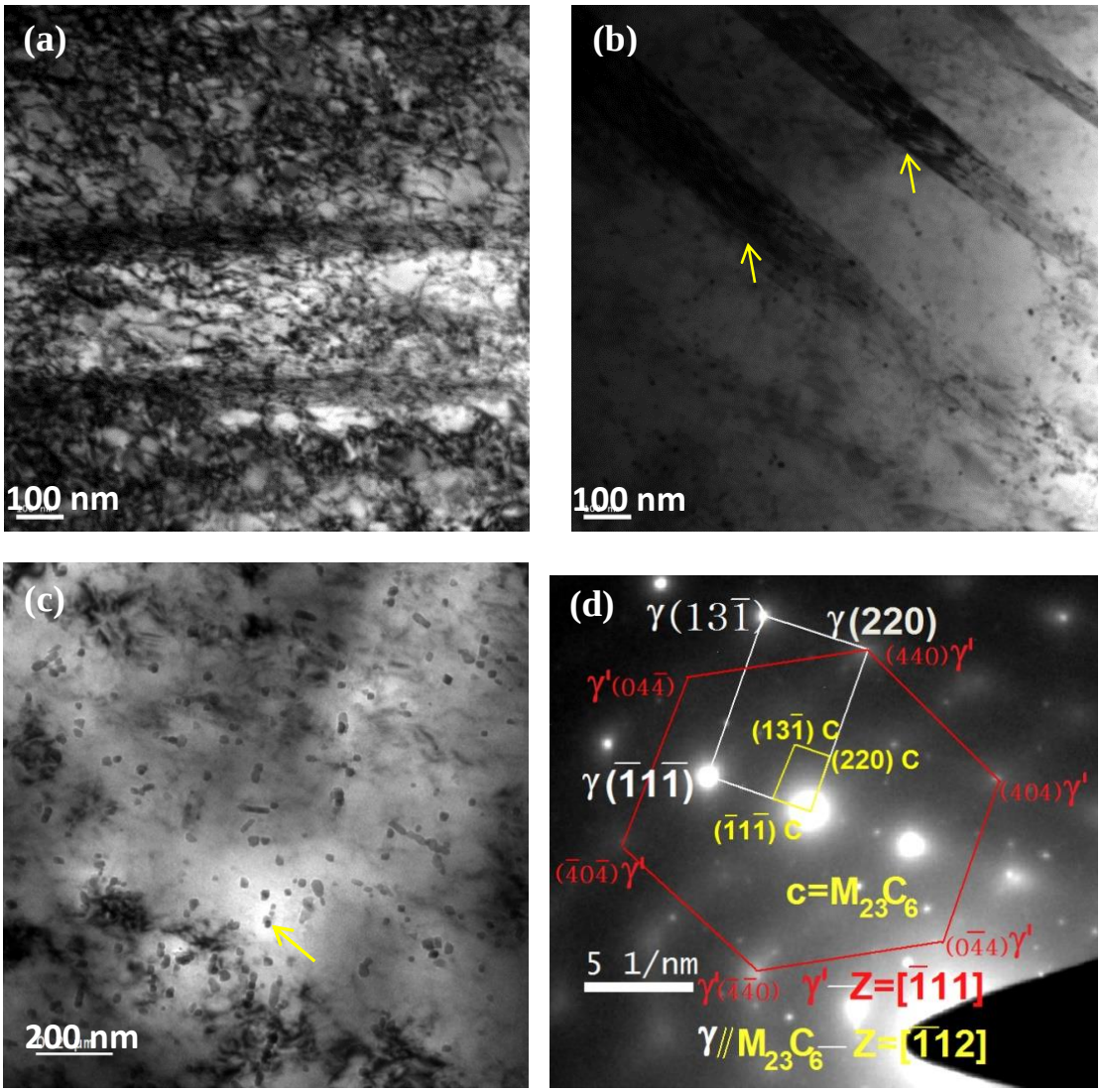

Fig. 3.21: TEM micrographs of tensile samples tested at 700^{o}C at a strain rate of 5x10^{-3} s^{-1} showing: (a) very few slip bands and high density of dislocations (b) micro twins observed (c) formation of very fine carbide ($M_{23}C_6$) and γ′ precipitates and (d) SAED pattern of the precipitates formed.

Figs. 3.22a and b show deformed microstructure of the sample tested at 800°C, above the DSA regime and reveal formation of the precipitates of $M_{23}C_6$ and sub grains during the deformation. SAED pattern shown in Fig. 3.22c confirms the precipitates as $M_{23}C_6$ carbides. The size of the precipitates (≈40-60 nm) is more than those found in samples tested at 700°C (less than 10 nm). Presence of γ′ is not observed at this temperature. No slip bands were observed in this case suggesting more uniform deformation process without localised persistent slip.

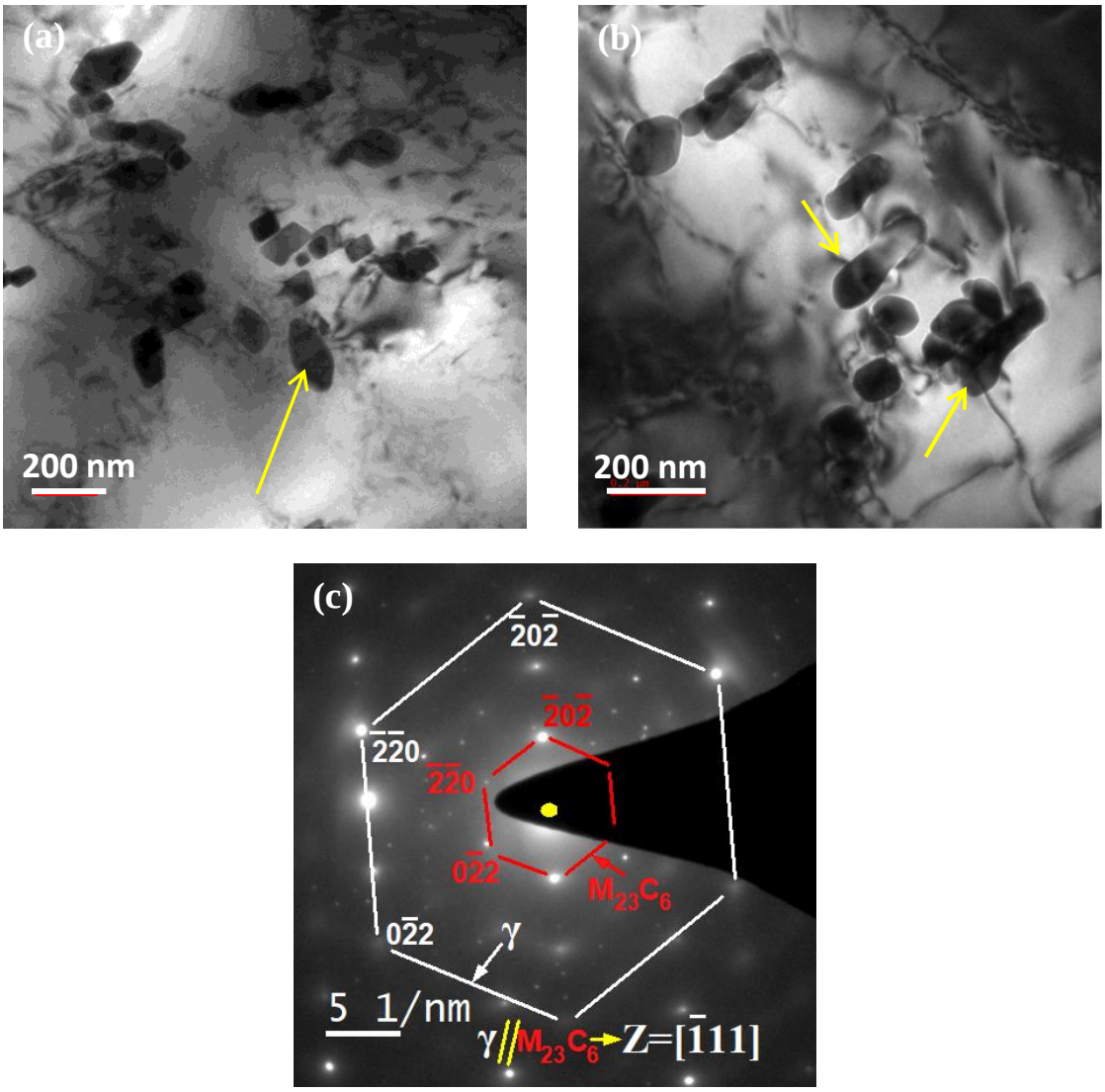

Fig. 3.22: TEM micrographs of tensile samples tested at 800°C (above the DSA regime) at a strain rate of $5x10^{-3}$ s^{-1} showing: (a) reprecipitation of carbides (b) precipitate dislocation interaction and (c) SAED pattern confirming the precipitates as $M_{23}C_6$ carbides.

3.11 Fracture Behaviour

The fracture surfaces of the tensile samples tested from RT to 900°C, at three different strain rates were examined to characterize the fracture behaviour. Fractographs of the specimens tested at the strain rate of $5x10^{-3}$ s^{-1} at room temperature, 400°C, 700°C and 800°C, without serrations, with serrations, ductility minima and no serrations respectively in Figs. 3.23 to 3.26 respectively. It is evident from these fractographs that there is significant difference in fracture behaviour of the material at different temperatures. At room temperature, the fracture surface (Fig. 3.23a) consists of dimples of varying sizes ranging from 5-15 μm, formed by coalescence of micro voids. The magnified view of the fractograph is given in Fig. 3.23b.

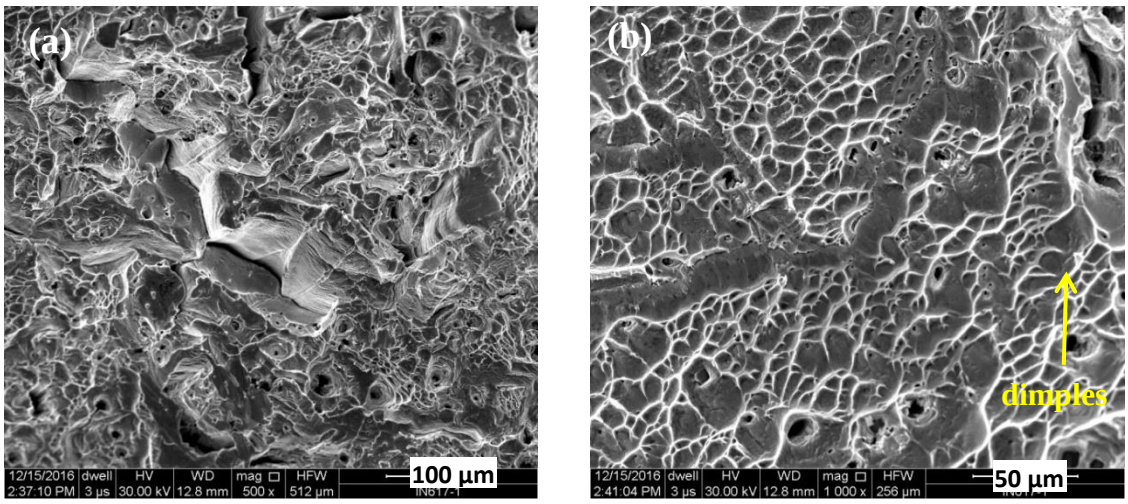

Fig. 3.23: SEM fractographs of tensile specimens tested at room temperature at strain rate of $5x10^{-3}$ s^{-1} showing: (a) full view and (b) high magnification image. Fracture surface shows dimples formed by micro void coalescence.

A completely ductile fracture with dimples is observed for the samples tested at 400°C (Fig. 3.24a). The size of the dimples is smaller (Fig. 3.24b) than those formed at room temperature, these dimples are about 3-5μm in size. At 700°C, the fracture surface shows much less fraction of ductile fracture with dimples as compared to that at room

temperature and 400°C. There number of facets is more (Fig. 3.25). Transgranular fracture occurred with formation of fine dimples and large facets.

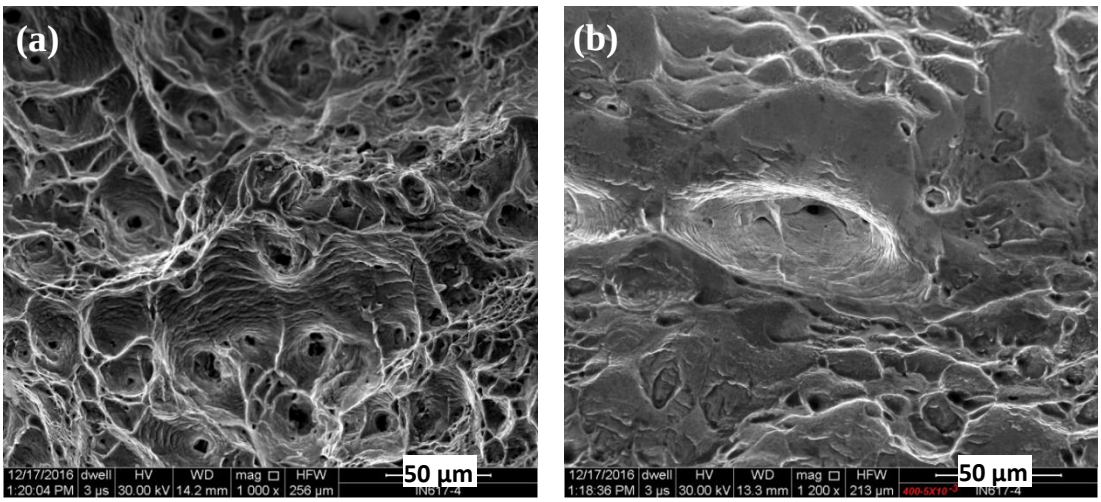

Fig. 3.24: SEM fractographs of tensile specimens tested at 400°C at strain rate of $5x10^{-3}$ s^{-1} showing: (a) dimples throughout the fracture surface (b) magnified view of the dimples.

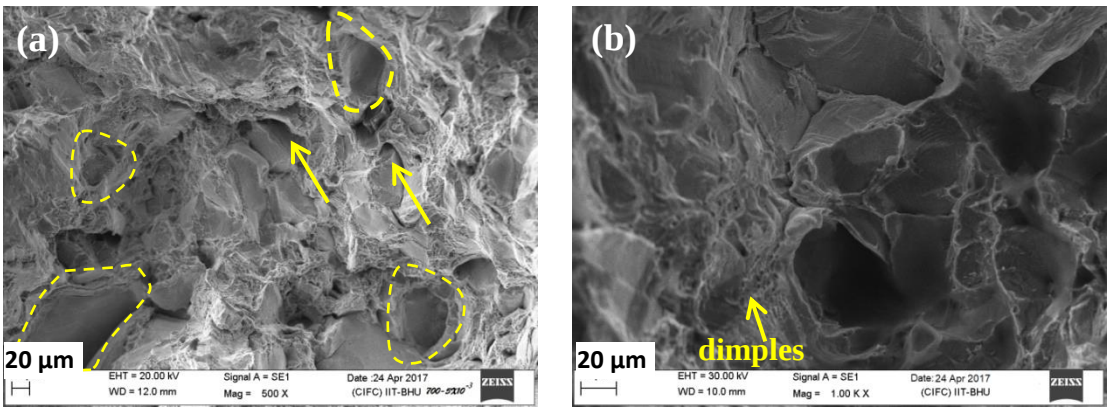

Fig. 3.25: SEM fractographs of tensile specimens tested at 700°C at a strain rate of $5x10^{-3}$ s^{-1} showing: (a) less number of dimples and more facets (marked regions), arrows indicates cracks observed (b) dimples in between faceted regions.

Figs. 3.26a &b show optical micrographs of the longitudinal sections of the samples tested at room temperature and 700°C respectively. While there is no sign of intergranular cracking at RT (Fig. 3.26a), there are some small intergranular cracks associated with grain boundaries of the specimen tested at 700°C (Fig. 3.26b).

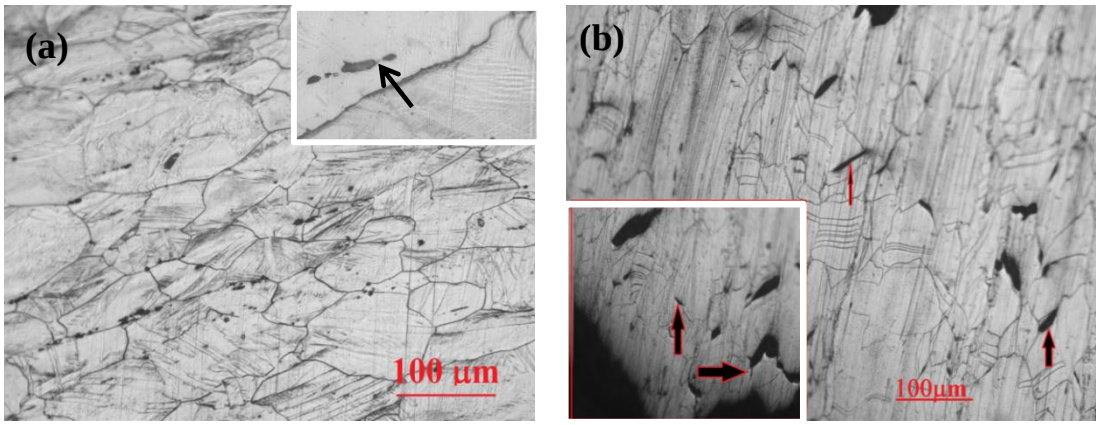

Fig. 3.26: Optical micrographs of longitudinal section of the tensile samples tested at: (a) room temperature showing voids and linkage of voids (see at the arrow) and (b) 700^{o}C showing small intergranular cracks along some grain boundaries (shown by arrow).

The fractographs in Fig. 3.27a &b show completely ductile fracture with distinct voids and dimples in the case of samples tested at 800^{o}C, the fracture surface becomes relatively more obscure by the oxide layer formed. At some locations (at the bottom of dimples), for the samples tested at lower temperatures, cracked particles of second phase may be seen (Fig. 3.28). EDS analysis of the particles revealed them to be carbides.

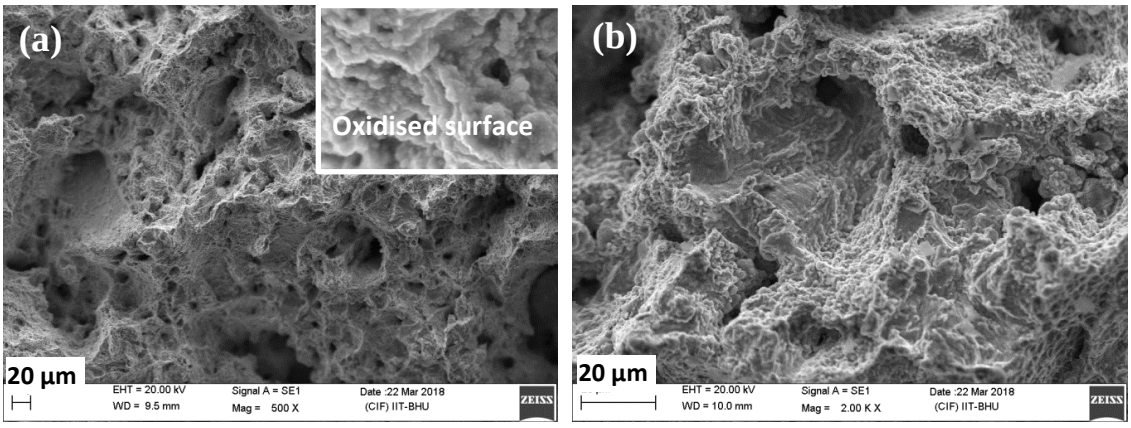

Fig. 3.27: SEM fractographs of tensile specimens tested at 800^{o}C at strain rate of 5x10^{-3} s^{-1} showing larger voids and dimples throughout the surface.

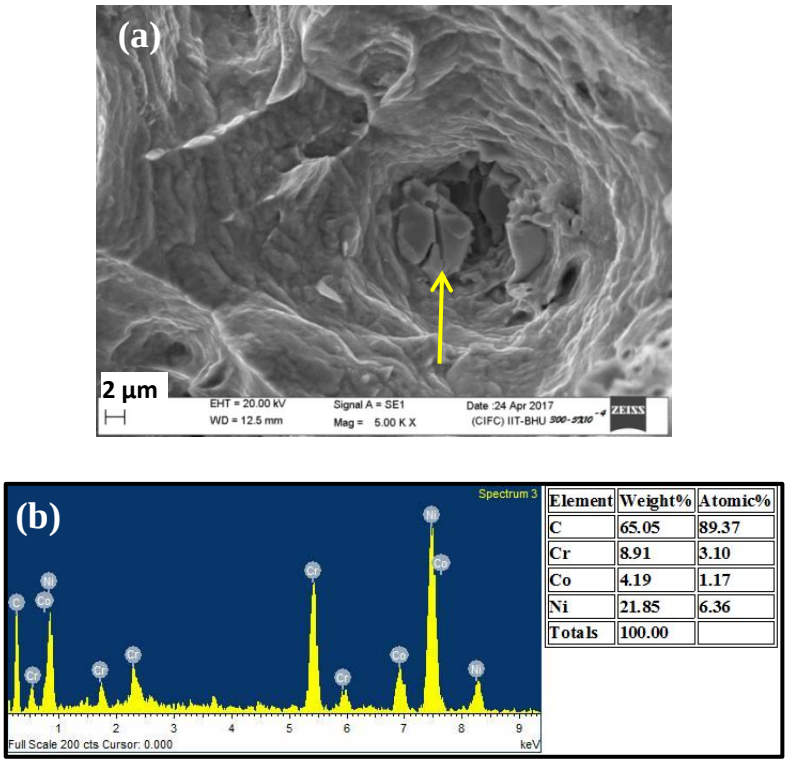

Element	Weight%	Atomic%
C	65.05	89.37
Cr	8.91	3.10
Co	4.19	1.17
Ni	21.85	6.36
Totals	100.00	

Fig. 3.28: (a) SEM fractograph of tensile specimen tested at 300^{o}C, showing cracked carbides (shown by arrow) and (b) EDS analysis of carbides present at the bottom of the voids.

3.12 Discussion

3.12.1 Dynamic Strain Aging

Serrated plastic flow was observed in the Inconel 617 alloy over the temperature range from 300^{o}C to 700^{o}C at all the strain rates studied. In addition, observation of plateau in the yield stress-temperature plots, peak in the flow stress (σ) with temperature, peaks in the rate of work hardening with temperature, negative strain rate sensitivity and ductility minima over this temperature range, suggest occurrence of DSA or Portevin Le Chatelier effect in this alloy. Based on the above manifestations, the temperature range for the DSA was established from 300^{o}C to 700^{o}C for this alloy. When mobile dislocations interact with solute atoms and form solute atmosphere around

dislocation core and pin them in the slip path. The pinning stress superimposes on the stress exerted by the dislocations and leads to an increase in the applied stress, which activates the movement of mobile dislocations. Due to the dynamic frictional stress drops, instability arises in the movement of dislocations back and forth between the slow and fast moving state. This is the main reason for the serrations to occur. The pinning of dislocations is discussed in the deformation behaviour with supporting TEM micrographs. The decrease in the critical plastic strain with increase in temperature can be attributed to ease of diffusion of solute atoms at higher temperatures facilitating the pinning process immediately at the beginning of plastic flow.

It is known that DSA occurs due to interaction of solute atoms and dislocations. The variables like strain rate and temperature affect the process of DSA. The increase in amplitude of the serrations, with increase in temperature, can be attributed to the faster diffusion rate of solute atoms at higher temperatures and formation of solute clusters around the mobile dislocations. When the strain rate is very high, then the velocity of mobile dislocations is much higher, hence the pinning action of solute atoms on mobile dislocations is quite low, and there is less effective DSA. On the other hand, with decrease in the strain rate, at appropriate temperature, interaction between solute atoms and dislocations increases, therefore the amplitude of the serrations increases. Lower strain rates provide sufficient time for effective pinning of movable dislocations. There is a specific range of temperature and the strain rate in which of the diffusion rate of solutes and the velocity of the dislocations are of the same order and there is a strong interaction between solute atoms and mobile dislocations and highly effective pinning action of solutes on mobile dislocations. However, when the temperature is much higher, the diffusion rate of solutes becomes very high, hence there is very less pinning actions of solutes on the mobile dislocations; therefore, the serrations disappear at very

high temperatures.

The plateau in the YS, the nearby constant value of the YS from 400 to 600^{o}C, is another manifestation of the DSA. Further increase in the yield strength at 800^{o}C is due to yield strength anomaly aspects as discussed by Roy et al. [33], which has been attributed to formation of precipitates around sub grains and grain boundaries. There is dissolution of carbides followed by re-precipitation in smaller size which increases the yield strength at this temperature. UTS, however, has shown a decline at all the temperatures and is accepted to be a normal phenomenon, though there is variation in the strain hardening parameters. The '*n*' value remains nearly constant up to 700^{o}C and decreases at higher temperatures (800^{o}C and 900^{o}C), reflecting low strength and low uniform strain. Though there is decrease in the *K* values at all the temperatures, the drop is very large at 800^{o}C and 900^{o}C due to recrystallization of grains and formation of new precipitate particles as reported by Roy et al. [33]. Elongation was found to have minimum values at 600 and 700^{o}C for all the strain rates. The degree of work hardening continuously increased with temperature up to 700^{o}C (Table 3.2) and suddenly decreased at 800^{o}C and 900^{o}C. The degree of work hardening in the DSA regime is found to be higher at in the present investigation as compared with those below and above the DSA region. Negative strain rate sensitivity exponent (*m*) promotes flow localization in the form of Lüder bands. Increased strain hardening enhances the probability of failure at such sites [31]. This is the prime reason for the ductility minima in the region of DSA where there is negative strain rate sensitivity. Any solute mobility will have a negative impact on the strain rate sensitivity and this increased with strain and temperature. When this strain rate sensitivity is negative, plastic flow becomes 'negative' and appears as serration in the stress strain curve [31].

A peak in the variation of work hardening rate with respect to temperature,

observed towards the upper end of the DSA, is in agreement with the fact that this temperature represents the conditions for strong pinning and hence the more rapid and stronger dislocation immobilisation. Further, it leads to increase in the rate of dislocation accumulation. Peaks were also observed in the rate of work hardening with respect to true stress, corresponding to the serrations that are observed in stress- strain curves. Precipitation of γ' and $M_{23}C_6$ has contributed for the high work hardening rate at 700^{o}C (peak).

DSA is a thermally activated process, its mechanism can be characterised by determining the values of activation energies for the different types of serrations and comparing these values with those reported in literature, with the diffusion coefficients of different elements. It is evident that variation in the types of serrations is controlled by the process of DSA. It is primarily controlled by the rate of diffusion of solute atoms, the concentration of solute atoms and densities of mobile and forest dislocations. As noted by Rodriguez [31], the value of the exponent ($m+\beta$) is often used to identify the mechanism or mechanisms responsible for the serrated yielding. It is generally accepted that when the exponent ($m+ \beta$) lies in the range of 0.5–1, interstitial solutes are responsible for strain aging, whereas when the value of ($m+ \beta$) is in the range of 2–3, substitutional solutes are responsible. Since the value of ($m+ \beta$) and the activation energy values for type B and (A+B) serrations for the temperatures up to 400^{o}C, are very close to those for the diffusion of interstitial carbon present in the γ matrix, the mechanism of serrated phenomena at the lower temperatures is based on the diffusion of interstitial carbon atoms [99]. At higher temperatures of 500^{o}C and 600^{o}C, where C type serrations were observed, the estimated activation energy is 101 kJ/mol, which is close to the activation energy for vacancy migration (106 kJ/mol). The activation energy for vacancy migration in Ni is calculated from the difference of the activation energy for

self-diffusion (280 kJ/mol) and the activation energy for vacancy formation (174 kJ/mol) [99, 100]. Therefore, it is suggested that formation of type C serrations is controlled by the migration of the substitutional solute atoms in the Inconel 617 alloy. The major substitutional elements are Cr, Co and Mo in this alloy hence diffusion of these elements could be considered to cause DSA over this temperature range [31, 93].

The strengthening of the material resulting from DSA caused increase in the yield strength and decrease in ductility in the present alloy. This strengthening due to DSA increased resistance of the material against fatigue crack initiation also. In general, in materials without DSA, the yield strength decreases with increase in temperature. However, in materials exhibiting DSA, the yield strength increases with increase in the temperature, in the range of DSA regime. This is reflected by hump or plateau in the stress-strain curve. Once the temperature increases beyond the range of DSA, the yield strength decreases and follows the usual trend as it is not affected by DSA. Low cycle fatigue life also decreases due to DSA because of reduction in ductility.

3.12.2 Deformation Behaviour

Distinct differences were observed in the configuration of dislocations in the samples tested from room temperature to 900^{o}C. Less number of slip systems operating at room temperature with very few tangles of dislocations, indicates lack of interaction of solute atoms with dislocations. The straight dislocation pile-ups observed, support a smooth movement of dislocations unhindered by the solute atoms. Similar features were observed in the samples tested at 200^{o}C, though there is a small increase in the tangles of dislocations. This observation is consistent with lack of serrations in the stress-strain curves in this temperature range. As the prominent serrated flow appeared in the stress-strain curves from 300 to 600^{o}C range, there is more pile-up of dislocations, formation

of dislocations cells. The cell size increased as the temperature was increased. There is an increase in the number of slip bands and decrease in the slip distance. At 700^{o}C, completely different deformation behaviour is observed. There is a less degree of pile-up of dislocations and formation of micro twins was observed. At this temperature there is increase in the diffusivity of solute atoms, precipitation of $M_{23}C_6$ and γ', and a decrease in the slip bands corresponding to minima in the ductility.

At higher temperatures increased atomic mobility and there in formation of saturated solute atmospheres around dislocations can be expected particularly in the DSA region. This causes rapid pinning of dislocations and there is a necessity of increasing applied stress to unpin these dislocations which results in a consequent increase in the density of dislocations. Bowing of dislocations and formation of dislocation kinks are further indicators of the increase in the hindrance caused to the movement of dislocations. The re-precipitation of carbides is a factor contributing to increase in the strength parameters at 800^{o}C as evidenced from the microstructures [33].

3.12.3 Fracture Behaviour

There is significant difference in the mode of fracture of the Inconel 617 alloy from RT to 900^{o}C as depicted in the Figs. 3.23 to 3.27. No necking was observed in the samples tested at RT to 700^{o}C whereas necking was clearly observed in the samples tested at 800 and 900^{o}C. Necking is also evident from the stress-strain curves and the necking strain. Transgranular fracture was exhibited with dimples and facets at room temperature. Ductile fracture with microvoid coalescence occurred at room temperature owing to the fact that grain boundary strength is high and deformation is concentrated within the grains. At 200-400^{o}C growth of a number of microvoids is observed. As the temperature is increased, because of serrated yielding and multiple slip systems being

operative, more number of voids of smaller size formed. The presence of carbides at the bottom of the voids, suggest that voids formed due to cracking of the carbides and also from the weak interface between the particles and the matrix.

At 600 and 700^{o}C with minima in ductility, even though there is ductile fracture with voids and dimples, there is also intergranular cracking, strain localization due to serrated yielding and reprecipitation of carbide particles are considered to be the prime factors for causing the ductility minimum [37]. As the interaction of dislocations with solute atoms and intergranular carbides or gamma prime particles leads to stress concentrations at the interface with the matrix, considerable deformation prior to fracture takes place with formation of voids at each location. At 700^{o}C the growth of these voids along the grain boundaries results in the observed facets and dimple rupture. The facets that are observed also contribute for ductility minima at these two temperatures. Fracture surface at 800^{o}C (above DSA) indicates complete ductile fracture and appreciable increase in the elongation. There is large amount of plastic deformation prior to fracture and the surface got oxidised and some tiny particles are observed throughout the surface.

3.13 Chapter Summary

The following observations can be summarized for the present chapter.

1. Dynamic strain aging occurs in Inconel 617 alloy in the temperature range from 300^{o}C to 700^{o}C at the strain rates $5x10^{-4}$ s^{-1}, $5x10^{-3}$ s^{-1} and $1x10^{-2}$ s^{-1}. The attendant serrations in the stress-strain curve are of the B, (A+B) and C type.
2. Critical plastic strain for the onset of serrations decreased with increase in temperature and reached a steady state at high temperatures. Plateau in the YS, peaks in the flow stress, ductility minima and negative strain rate sensitivity are

the various manifestations of DSA phenomenon exhibited by the Inconel 617 alloy. UTS decreased with increase in temperature for all the three strain rates mentioned.

3. Ludwigson equation is found to be the best relationship to describe the flow behaviour of this alloy. Strength coefficient, *K* and strain hardening exponent, *n* values decreased with increase in temperature. Peaks were observed in the variation of rate of work hardening with temperature and with the true stress.
4. The average activation energies for the serrated flow are calculated as 65 kJ/mol, 80 kJ/mol, and 101 kJ/mol for the three types of serrations mentioned above. The controlling mechanism of DSA is suggested to be diffusion of carbon through dislocation cores in the lower temperature range and those of substitutional elements Cr and Mo in the higher temperature range from the above activation energy values.
5. TEM study revealed increase in the number of slip bands with increase in temperature and a decrease in dislocation density with increase in temperature. Interaction of dislocations with solute atmospheres increased with increase in temperature in the DSA region. Precipitation of $M_{23}C_6$ and γ' particles was observed at 700^{o}C whereas only carbides were present at 800^{o}C.
6. SEM examination of fracture surfaces showed transgranular mode with dimples at room temperature. In the range of 400-600^{o}C, there was complete ductile fracture. At 700^{o}C, mixed mode of fracture with dimples, facets and intergranular cracks associated with some grains boundaries observed causing ductility minima at this temperature.